Suppression of conformational heterogeneity at a protein–protein interface

Lindsay N. Deis, Qinglin Wu, You Wang, Yang Qi, Kyle G. Daniels, Pei Zhou, and Terrence G. Oas[1]

Department of Biochemistry, Duke University, Durham, NC 27710

Edited by Ken A. Dill, Stony Brook University, Stony Brook, NY, and approved June 8, 2015 (received for review December 24, 2014)

Staphylococcal protein A (SpA) is an important virulence factor from *Staphylococcus aureus* responsible for the bacterium's evasion of the host immune system. SpA includes five small three-helix–bundle domains that can each bind with high affinity to many host proteins such as antibodies. The interaction between a SpA domain and the F_c fragment of IgG was partially elucidated previously in the crystal structure 1FC2. Although informative, the previous structure was not properly folded and left many substantial questions unanswered, such as a detailed description of the tertiary structure of SpA domains in complex with F_c and the structural changes that take place upon binding. Here we report the 2.3-Å structure of a fully folded SpA domain in complex with F_c. Our structure indicates that there are extensive structural rearrangements necessary for binding F_c, including a general reduction in SpA conformational heterogeneity, freezing out of polyrotameric interfacial residues, and displacement of a SpA side chain by an F_c side chain in a molecular-recognition pocket. Such a loss of conformational heterogeneity upon formation of the protein–protein interface may occur when SpA binds its multiple binding partners. Suppression of conformational heterogeneity may be an important structural paradigm in functionally plastic proteins.

Staphylococcus aureus virulence | conformational heterogeneity | staphylococcal protein A | X-ray crystallography | immunoglobulin Fc binding

The Gram-positive bacterium *Staphylococcus aureus* is commonly found on the skin and in the respiratory tract and can cause a variety of health complications ranging from skin lesions and boils to more serious infections such as sepsis and endocarditis (2, 3). Staphylococcal protein A (SpA) is an important virulence factor found on the surface of *S. aureus* cells. This 42-kDa protein has two functional halves: the N-terminal half, which consists of five protein-binding domains (E-D-A-B-C) with high sequence identity that are each able to bind to many different partner proteins, and the C-terminal half, which is responsible for anchoring the protein in the cell wall.

SpA has a wide range of functions that require binding to many target proteins in the host during infection (Fig. 1). One such target is tumor necrosis factor receptor 1 (TNFR1), which binds to residues on helix 1 (F5, F13, Y14, and L17) and helix 2 (I31 and K35) on all five SpA protein-binding domains and competes for antibody binding (4). SpA binding mimics TNF-α activation of airway cells, leading to inflammation (5). SpA also binds the A1 domain of the hemostasis protein von Willebrand factor (vWf) with 15-nM affinity (6) using residues on helix 1 (Q10, F13, Y14, and L17) and helix 2 (N28, I31, and K35), which allows *S. aureus* to adhere to surfaces (7).

In addition to its roles in inflammation and platelet adhesion, SpA also assists *S. aureus*'s adept evasion of the immune system by binding host IgG and IgM antibodies. Each SpA domain can bind both F_c and F_{ab} fragments, with SpA's affinity for F_c (K_D 10–30 nM) ~30-fold tighter than that for F_{ab} (8, 9). This unusual mode of antibody binding inhibits binding of the F_c subunit to the host phagocyte F_c receptor, thereby protecting the bacterial cell from phagocytosis (10).

The SpA domain–F_c interaction was partially elucidated previously in the crystal structure 1FC2 to 2.8-Å resolution (11). In this structure, the SpA B domain (SpA^B) binds to the hinge region between the CH2 and CH3 domains of F_c. The SpA side of the interface is the helix 1/2 face of SpA^B, which makes many contacts with the antibody at S254, Q311, L432, and N434. The residues on the SpA-domain side that contact F_c reside on helix 1 (F5, Q9, Q10, N11, F13, Y14, and L17) and helix 2 (N28, I31, Q32, and K35) (11). The 1FC2 structure guided subsequent mutagenesis experiments from other groups. A two-helix derivative of an engineered SpA^B with selected substitutions bound to F_c with comparable affinity to the wild-type domain (12). In another study, mutation of other key residues, including the Q9K/Q10K/D36A/D37A variant of SpA^B, greatly reduced the affinity of SpA^B for F_c (13).

SpA domains also bind the F_{ab} fragments of antibodies, albeit also not at the canonical antigen-binding interface. A crystal structure of the SpA D domain (SpA^D) in complex with F_{ab} from IgM at 2.7-Å resolution (PDB ID code 1DEE) showed that a VH region forms the SpA interface (10). On the F_{ab} side, this interface is formed by framework β-strands and interstrand loops that are distant from the antigen-combining site. The interaction between SpA domains and F_{ab} is thought to contribute to selection of VH3-encoded B-cell antigen receptors (14), as well as suppression and deletion of B lymphocytes (15) as a consequence of *S. aureus* infection. SpA^D residues involved in binding F_{ab} reside on helix 2 (Q26, G29, F30, Q32, S33, and D36) and helix 3 (N43, E47, and L51) (10). These residues are distinct from the residues bound to F_c in the 1FC2 structure.

Significance

The emergence of antibiotic-resistant strains of bacteria, such as methicillin-resistant *Staphylococcus aureus*, is an increasing threat to human health. *S. aureus* infections cause a variety of health complications, ranging from skin lesions to life-threatening infections. Staphylococcal protein A (SpA) is the major cell-surface protein and a multitarget virulence factor. The design of SpA-targeted therapeutics requires a molecular description of its interactions with host proteins. Here we report the crystal structure of a complete SpA domain in complex with an F_c fragment of human IgG. Our structure reveals changes in SpA when it binds to F_c, including a significant reduction in conformational heterogeneity as well as displacement of a SpA side chain by an F_c side chain in a molecular-recognition pocket.

Author contributions: L.N.D., Q.W., P.Z., and T.G.O. designed research; L.N.D., Q.W., Y.Q., and K.G.D. performed research; Y.W., Y.Q., K.G.D., and P.Z. contributed new reagents/analytic tools; L.N.D., Q.W., Y.Q., K.G.D., and P.Z. analyzed data; and L.N.D., Q.W., and T.G.O. wrote the paper.

The authors declare no conflict of interest.

This article is a PNAS Direct Submission.

Data deposition: The crystallography, atomic coordinates, and structure factors reported in this paper have been deposited in the Protein Data Bank, www.pdb.org (PDB ID codes 4WWI, 4ZMD, and 4ZNC).

[1]To whom correspondence should be addressed. Email: oas@duke.edu.

This article contains supporting information online at www.pnas.org/lookup/suppl/doi:10.1073/pnas.1424724112/-/DCSupplemental.

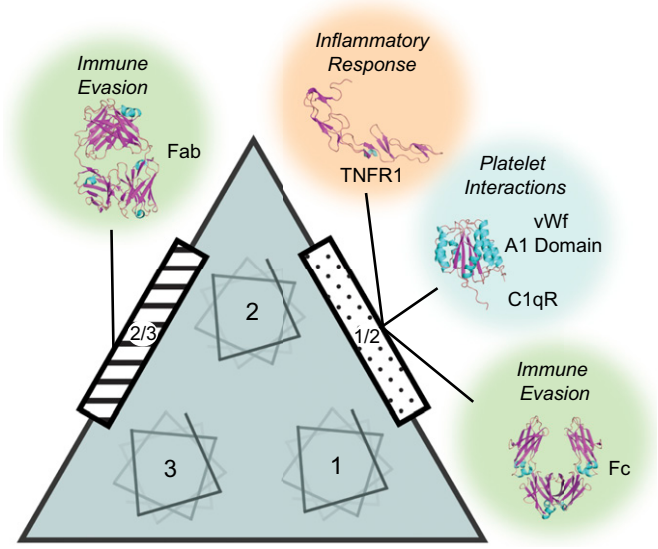

Fig. 1. Various SpA binding partners and their corresponding binding interfaces on the SpA molecule. The majority of partner proteins, including F_c, bind to the helix 1/2 interface. F_{ab} binds to the helix 2/3 interface. One of the interactions seen in the current structure also involves this interface.

We previously reported the ultra-high–resolution crystal structures of SpA^C and $SpA^{B\text{-}B}$ (two SpA B domains connected by the conserved linker) (16). These structures exhibited extensive conformational heterogeneity, with many concerted conformational changes both at the residue level and at the tertiary-structure level. Over 60% of residues in each structure contained alternative conformations of either backbone or side chain. In addition, helix 1 assumed many different poses, both within each structure as alternative conformations and among structures, both ours and those previously reported. If this enhanced heterogeneity of helix 1 is also present in SpA domains in solution, it may be responsible for the functional plasticity at the helix 1/2 interface, which binds many different partner proteins.

As a very early structure of an antibody molecule in complex with another protein, the original 1FC2 F_c–SpA^B structure was seminal (11). However, this work left many substantial structural and functional questions unanswered. In addition, helix 3 of the three-helix–bundle SpA^B was folded irregularly in the 1FC2 structure. This observation initially led investigators to speculate that unfolding of one of the three helices was concomitant with binding. Subsequent NMR-detected amide exchange studies (17–19) showed that all three helices are fully formed when the SpA domain is bound to F_c in solution, indicating that the absence of a folded helix 3 in the 1FC2 structure is likely a crystallization artifact. Structure determination of the complex by NMR has not been possible to date. Thus, a detailed description of the changes in conformational heterogeneity in the SpA domain that take place upon binding F_c has remained unresolved before the structure we report here. Does the ability of SpA domains to bind multiple proteins at the same site stem from a capacity to suppress conformational heterogeneity at a partner-specific complementary interface? What role does displacement of intramolecular side chains play upon binding of F_c? These questions were not addressed by either the previous apo NMR structures or the 1FC2 crystal structure. The structure we report here provides some key answers.

To investigate the detailed conformational state of SpA domains when bound to F_c, we solved the structure of SpA^C in complex with F_c at 2.3-Å resolution (Fig. 1). The structure shows that both interfacial and noninterfacial SpA^C residues have decreased conformational heterogeneity compared with the apo structure. In addition, we have successfully decreased affinity of SpA^C for F_c by prefilling a molecular-recognition pocket with a Q9W substitution. This hydrophobic pocket is filled intramolecularly by the F5 ring in the WT apo structure, but this side chain is displaced by I253 of F_c in the complex. We have solved the crystal structures both of apo SpA^C Q9W and of SpA^C Q9W bound to F_c. Our results suggest that a small-molecule drug bound to this pocket could hinder antibody binding in a similar way.

Results and Discussion

Overview of the F_c–SpA^C Complex Structure. To elucidate the atomic-level details of SpA^C when bound to the F_c fragment of IgG, we crystallized both proteins in complex with one another. An intact IgG in vivo includes two chains of F_c linked by two disulfide bonds at the C-terminal end of the domain, which together form a dimeric IgG fold at the N-terminal end. To facilitate correct disulfide formation, we truncated the protein before the two C-terminal cysteines to produce an unlinked single F_c chain (hereafter referred to as "F_c monomer").

Tetragonal bipyramidal crystals of the F_c–SpA^C complex grew in the space group *C*2 (*Experimental Procedures*). Diffraction data were collected to 2.3-Å resolution at cryogenic temperatures and solved by molecular replacement using SpA^C from PDB ID codes 4NPD (16) and 1FC2 (11) as the search models (Table S1). The asymmetric unit contains three molecules of SpA^C (chains A–C) complexed with three molecules of F_c monomer (chains D–F). The three F_c monomers have a mean pairwise rmsd value of 0.26 Å, as do the three SpA^C molecules. Despite being purified as a single chain, each F_c monomer in the structure forms a dimer with another F_c monomer to form the typical IgG fold. Fig. 2 depicts an F_c dimer in complex with four SpA^C molecules. The F_c loops distant from the IgG fold are conformationally diverse and have poor electron density, and no density was observed for the C-terminal F_c 6×His tag.

Comparison of the New Structure with the Previous 1FC2 Structure. There are several similarities between the 1FC2 structure and the one reported here. The three SpA^C molecules in our

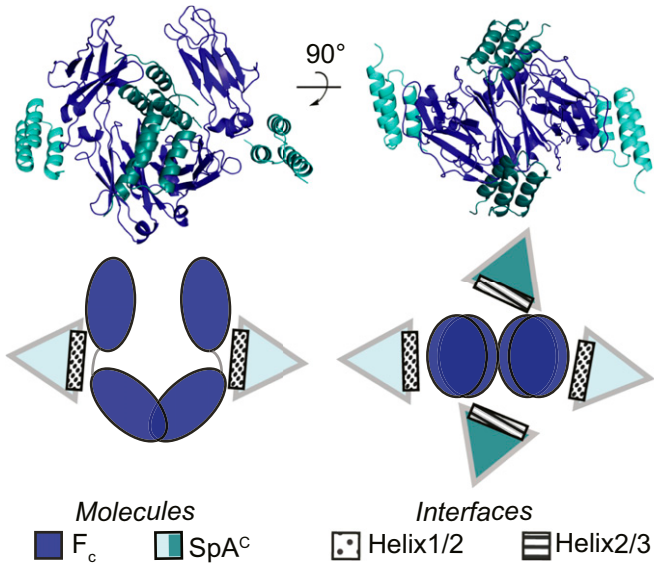

Fig. 2. New F_c–SpA^C cocrystal structure at 2.3 Å. Despite missing the two disulfide-forming C-terminal cysteine residues, the F_c molecules (blue) form a dimer with the canonical IgG fold. Two SpA^C molecules (light cyan; *Left*) use the helix 1/2 interface (dots) described previously (11). The new previously unobserved interface is formed with the helix 2/3 face of two other SpA^C molecules (turquoise), shown in ribbon and cartoon form (*Right*).

structure bind to F_c at the previously described location (11), at the hinge between the CH2 and CH3 domains of F_c (Fig. S1*A*). Also, the global F_c fold matches that seen in 1FC2. The CH2 and CH3 domains each superimpose well, with mean rmsd values of 0.48 and 0.43 Å, respectively. However, the mean rmsd value for the entire F_c monomer rises to 0.64 Å, presumably because the angle between the CH2 and CH3 domains is larger in 1FC2 than in the current structure. In addition, the individual C-terminal loops in the 1FC2 structure also adopt slightly different conformations from in the current structure, and any differences in loop conformation are likely due to crystal packing. These loops have not been implicated in binding to SpA and, therefore, do not affect analysis of the complex.

Although the F_c molecules from the new complex and from 1FC2 adopt very similar conformations, the biggest difference between the two structures is on the SpA-domain side. The F_c interface, formed from helix 1 and helix 2 of SpA^B, is properly folded in 1FC2. However, residues 42–47 were folded irregularly in the old structure and, therefore, not modeled as a helix, and residues 48–58 were not modeled at all (11). Consequently, no information is available about the true structure or conformational heterogeneity of one-third of the SpA domain in 1FC2. In the new structure, all three helices are properly folded. Another difference between the current complex structure and 1FC2 is the SpA-domain sequence. The current structure includes a SpA^C domain, whereas 1FC2 has SpA^B. However, only five residues differ between the two domains (Fig. S1*B*). N/T23, A/K42, and L/I44 are not involved in an interface, and Q/V40 and N/E43 are not involved in the primary (helix 1/2) interface.

Residues at the Helix 1/2 Interface Undergo Concerted Conformational Changes upon F_c Binding. Previously, we showed that SpA domains are conformationally heterogeneous throughout, both at the individual-residue level and at the tertiary-structure level (16). The interfacial residues (Q10, F13, Y14, L17, H18, and I31) for the F_c-binding site are particularly heterogeneous, with multiple identifiable backbone and side-chain conformations in the electron density. In the current structure, electron density for the helix 1/2 interfacial residues is clearly represented by a single model (Fig. 3*A*) where each residue has only one side-chain rotamer at both 1σ (purple mesh) and 0.3σ (gray surface) electron density. Therefore, the interacting residues on helix 1/2 apparently adopt a single conformation to form an interface that is compatible with the F_c molecule.

Previous work comparing the apo SpA^C structure with the 1FC2 structure suggested that concerted rotamer changes were needed for compatible F_c binding. To update this comparison with our new structure, we superimposed the helix 1/2 interface of our F_c–SpA^C complex structure onto the 4NPD SpA^C (orange) and 4NPF $SpA^{B\text{-}B}$ chain X (green) structures (Fig. 3*B*). Whereas the majority of residues in SpA^C remain conformationally diverse outside of the interface, each of the six helix 1/2 interfacial residues adopts a single rotamer in the complex. The most drastic change is at Y14, whose ring swings 180° away from the tyrosine ring in apo SpA^C. The apo $SpA^{B\text{-}B}$ structure captures both of these rotamers (16).

Conformational Heterogeneity of SpA^C Is Significantly Reduced in the Complex, Particularly in Helix 1/2 Interfacial Residues. The new SpA^C–F_c complex structure at 2.3 Å has poorer resolution than the apo SpA^C structure at 0.9 Å, making it difficult to compare the conformational heterogeneity between the two structures by simply counting the number of alternative conformations. At high resolution, the maximum distance between equivalent atoms of alternative conformations is a convenient measurement of the conformational heterogeneity. However, at poorer resolutions, where discrete alternative conformations may not always be visible, another metric must be used to quantify the conformational heterogeneity. The electron-density map value is one such metric. By comparing the ratio of the backbone and side-chain electron-density map values, hereafter referred to as the "ρ ratio" (R_ρ), one can compare the conformational heterogeneity between structures of varying resolutions.

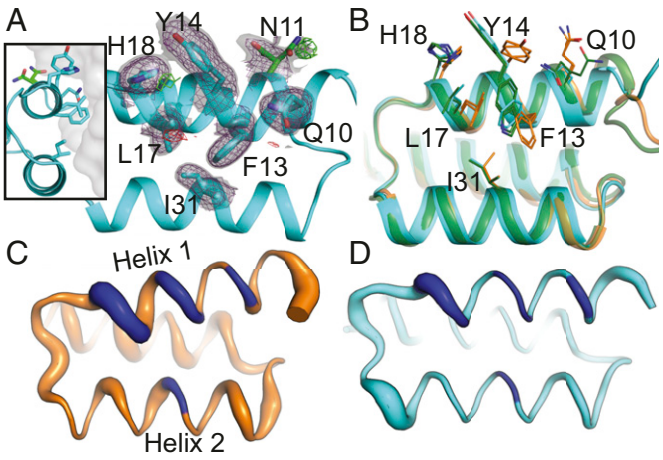

Fig. 3. Rotameric heterogeneity of interfacial residues (blue) is suppressed in the complex. (*A*) Helix 1/2 interfacial residues (cyan) adopt single rotamers in the complex, as exhibited by their electron density at both 1σ (purple mesh) and 0.3σ (gray surface). (*Inset*) SpA^C helix 1/2 interface formed with F_c (gray). Conformational heterogeneity is still detected in the electron density at N11 (green), a noninterfacial residue, and is confirmed by a +3σ or −3σ difference map (green and red mesh, respectively). (*B*) Helix 1/2 interfacial residues are heterogeneous in apo SpA^C (orange) and $SpA^{B\text{-}B}$ (green) but freeze into single conformations in the complex (cyan). (*C* and *D*) Putty diagram for apo SpA^C (*C*) and SpA^C in complex with F_c (*D*), where the relative diameter of the putty represents the ρ ratio (see text).

To quantify the conformational heterogeneity for all residues except alanine and glycine, which have no side-chain rotamers, we calculated $R_\rho = (\rho_{C\alpha} - \rho_{C\chi})/\rho_{C\alpha}$, where ρ_{CX} is the value of the $2F_o - F_c$ map for carbon atom X in electrons per $Å^3$ using *phenix.map_value_at_point* with the default resolution_factor (20). For residues with more than one C_χ atom, the average C_χ map value was used. Because backbone contour levels are usually greater than or equal to the side-chain levels, R_ρ ranges from 0 (no difference between backbone and side chain) to 1 (no detectable side-chain density). R_ρs for chain A of the complex and for the SpA^C apo structure are listed in Table S2 and depicted as putty diagrams in Fig. 3 *C* and *D*, respectively, where the relative diameter of the putty represents the ρ ratio. Side chains that form the helix 1/2 interface, shown in blue, are conformationally heterogeneous in the apo structure, but this rotameric conformational heterogeneity is frozen out in the complex structure, as indicated by a thin putty diameter.

Apo SpA^C Has Similar Side-Chain Conformational Heterogeneity in Solution and Crystals. We performed three-bond scalar coupling (^3J) experiments on $^{13}C/^{15}N$ SpA^C in the absence of F_c to compare the conformational dynamics leading to ^3J and/or chemical shift averaging in solution (21–23) with the conformational heterogeneity previously observed in crystals of SpA^C (16). Data for $^3J(C\gamma C')$, $^3J(C\gamma N)$, and $^3J(C\delta_1 C\alpha)$ were recorded using standard methods (*Experimental Procedures*). Stereo-specific assignments were determined for Leu and Val residues based on the assumption that the crystal structures and solution structures share the same predominant rotamer conformation. In addition, the chemical shifts of δ_1 carbons of isoleucine residues and the differences in chemical shifts for the δ_1 and δ_2 carbons of leucine residues were used to determine the extent of averaging due to rotation around the χ_2 angle. These data are summarized in Table S3 for the 14 residues that yielded observations. Of the 14 residues, 8 show at

least two alternate conformations in the apo SpA^C crystal structure and have dynamics in χ_1 or χ_2 by NMR. Two of these, L17 and I31, are found at the F_c interface and lose their conformational heterogeneity in the crystal structure of the complex, as judged by the lack of alternate side-chain conformations detected by qFit (24) and by their low ρ ratios (0.24 and 0.13, respectively). Unfortunately, the 4 remaining interfacial residues were not among the 14 side chains whose dynamics were observable in our NMR experiments, so the loss in heterogeneity observed in the crystal structures for these residues has not been confirmed by NMR. Two of the 14 residues observed by NMR (L22 and V40) show no side-chain dynamics in solution or in crystals. Of the remaining 4 residues a missing assignment precludes comparison for K49, and the other 3 residues have discrepancies between solution and crystals. I16 has a single conformation in multiple SpA-domain crystal structures, whereas its χ_2 angle appears to be dynamic, with predicted gauche- and trans populations of 0.2 and 0.8, respectively (25). Likewise, L45 has a single conformation in crystal structures but has a dynamic χ_2 angle, with trans and gauche+ populations of 0.43 and 0.57, respectively (26). Apparently crystallization reduces the dynamics in these two residues. Finally, T23 appears to be dynamic by NMR but has only one conformer in crystals. This side chain forms a crystal contact in the SpA^C structure, which may freeze out its dynamics. The general agreement between NMR-detected side-chain dynamics of SpA^C in solution and the rotameric heterogeneity observed in crystals lends further support to our observation that rotameric heterogeneity is greatly reduced from SpA^C in the apo state to form the SpA^C–F_c complex. Such a reduction in heterogeneity is similar to that observed in the multifunctional proteins ubiquitin (27) and calmodulin (28).

F_c Forms a Second Interface on the Helix 2/3 Side of SpA^C. Although the new structure includes the same helix 1/2 SpA^C interface from the 1FC2 structure, two SpA^C molecules also bind to the F_c dimer on their helix 2/3 interfaces (Fig. S2). On the F_c side of this previously unidentified binding interface, the orientation of the IgG fold relative to SpA^C differs greatly from that of F_{ab} in the 1DEE F_{ab}–SpA^D complex (10). The SpA^D is bound to the VH domain of F_{ab}, whereas the SpA^C at the previously unidentified interface interacts with the hinge region of F_c (Fig. S2*A*). However, whereas the binding modes for the IgG fragments are quite different, the interfaces on the SpA-domain side are homologous. Both F_{ab} and F_c bind at the helix 2/3 interface of SpA. The majority of SpA^C residues involved in binding F_c at this interface are the same as the SpA^D residues that bind to F_{ab}. These residues adopt very similar rotamer conformations in both complex structures (Fig. S2*B*).

Previous isothermal titration calorimetry (ITC) studies indicated that F_c binds to full-length SpA with a stoichiometry of 2.35 ± 0.32 (8). However, because SpA contains five individual protein-binding domains that each may bind to multiple proteins simultaneously, it is difficult to tease apart the stoichiometry for individual domains. Therefore, we measured the binding stoichiometry at 5 μM via ITC by titrating F_c into SpA^C (Fig. S3*A*) and SpA^C into F_c (Fig. S3*B*). Both binding isotherms were simultaneously fit to obtain a stoichiometric ratio of ∼1.1 (Fig. S3*C*). However, the K_D cannot be accurately estimated, because the *c* value (29) is much greater than 100 at 5 μM. We estimate that the K_D is at least 10 nM or tighter, which is consistent with previous estimates (8).

To determine the minimal affinity detectable by our ITC experiments, we simulated two-site isotherms using the best-fit K_D value for the tight site and various K_d values for the second binding site (Fig. S3*D*). The second binding site was only apparent in the simulated isotherms if the second-site K_D was 10 μM or tighter. The concentration of F_c in our crystallization conditions was 100–200 μM. On this basis, we conclude that the second-site K_D must be in this range and, therefore, the interface we observe in our crystals between SpA^C helix 2/3 and F_c is a low-affinity interaction that would occur only at high local concentrations of both proteins. It may be that such high local concentrations could occur when antibodies are bound at the *S. aureus* cell surface, which could make the helix 2/3-binding site functionally relevant.

SpA Contains an Important Molecular-Recognition Pocket for F_c. A detailed analysis of the atomic interactions between SpA domains and F_c provides key insights into the binding reaction and its structural determinants. The improved resolution of our F_c–SpA domain complex structure allows us to visualize previously unidentified side-chain interactions. In particular, F5 undergoes a large rotamer change (Fig. 4*A*). In the apo structure (orange sticks), the aromatic ring nestles into a pocket between Q9 of helix 1 (green sticks) and the C-terminal end of helix 2. The placement of the ring is supported by NOEs observed in the solution structure on another SpA domain between F5 and nearby residues [BioMagResBank (BMRB) accession no. 4023 (30)], depicted as dashes. However, in the complex structure, F5 flips outward to accommodate F_c I253, which makes van der Waals interactions with the same pocket. F5 docking and displacement are facilitated by the flexibility of its backbone. We hypothesized that substitution

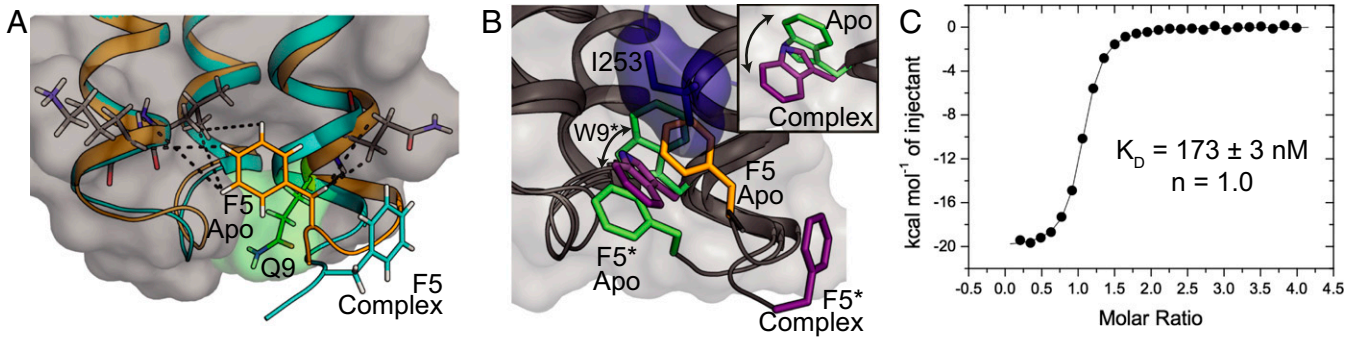

Fig. 4. Role of the SpA molecular-recognition pocket in F_c binding. (*A*) F5 in apo SpA^C (orange) nestles into a pocket between Q9 (green sticks) and the C-terminal end of helix 2. Dashes represent NOEs measured previously in solution between F5 and nearby residues (BMRB accession no. 4023) that confirm F5 placement (23). F5 in the complex (cyan) flips outward, making the pocket accessible to F_c. (*B*) Prefilling of the molecular-recognition pocket by the Q9W substitution (indicated by an asterisk) displaces F5* in apo Q9W (green sticks). The W9* indole ring adopts a favorable rotamer that would sterically block F_c I253. (*Inset*) W9* must flip to a less-favorable rotamer (purple sticks) when bound to F_c. (*C*) The affinity of SpA^C Q9W for F_c is 17-fold weaker than in wild-type SpA^C as measured by ITC.

of nearby Q9 with a bulky tryptophan might prefill the pocket and lower the affinity of F_c for SpA.

To test this hypothesis, we solved the crystal structure of apo SpA^C Q9W (Table S4), which contains two chains of SpA^C Q9W in the asymmetric unit. To avoid confusion with the wild-type structure, all residues from SpA^C Q9W are labeled with an asterisk (*). Just as I253 displaces F5 in the wild-type complex, W9* displaces F5* in both chain A (green sticks in Fig. 4*B*) and chain B of the Q9W variant, causing the F5* side chain and backbone to flip outward. The W9* indole ring adopts a favorable rotamer (50% rotamericity) and fills the pocket in a way that would sterically block F_c I253 from binding. Just as in wild-type SpA^C, we measured the affinity constant K_D and the binding stoichiometry at 5 μM via ITC by titrating SpA^C Q9W into F_c (Fig. 4*C*). The binding isotherm was fit to obtain an n value of 1.0 ± 0.006 and a K_D of 170 ± 3 nM (*c*, 29), which is 17-fold weaker than the maximum value we estimated for the K_D of wild-type SpA^C (see above).

To understand the structural basis for this reduction in affinity, we solved the crystal structure of SpA^C Q9W in complex with F_c (Fig. 4*B* and Table S5). I253 in the Q9W complex binds to the same pocket as it does in wild-type SpA^C and adopts the same rotamer. However, binding of I253 to the F5 pocket requires the W9* side chain to flip outward and adopt a less-favorable rotamer (12% rotamericity). This observation suggests that a small-molecule drug bound to this pocket would hinder I253 binding in a similar way, thereby significantly reducing the affinity for antibody. Such a small molecule could serve as both a novel therapeutic for combating *S. aureus* infection and as an important biotechnology tool for purifying antibodies by allowing displacement of antibodies from SpA columns at higher pH.

The helix 1/2 interface on SpA domains can bind many proteins, including the F_c fragment of IgG (9), TNF-α receptor 1 (5), von Willebrand factor (6), and the C1qR component of complement (31). We previously reported the enhanced conformational heterogeneity at the helix 1/2 interface of SpA^C, which may help SpA accommodate multiple binding partners (16).

The enhanced heterogeneity at the helix 1/2 interface and throughout the protein suggests that binding is coupled to rotameric conformational changes, which presumably are required for binding of other partner proteins, such as TNFR1 and vWf, to this interface. The virulence conferred by SpA is a direct result of its ability to bind many protein partners. SpA domains could possibly bind multiple antibodies simultaneously, F_c at the heterogeneous helix 1/2 interface and F_{ab} at the helix 2/3 interface. It is also possible that the second binding site we observed in our structure may play a role in polyvalent antibody binding when primary-site binding raises the effective concentrations of both proteins. This polyvalent binding strategy is frequently observed at cell surfaces, and may play a key role in the ability of *S. aureus* to evade the host immune system.

Future studies of this system will seek to confirm and further quantitate the binding-induced loss in conformational heterogeneity on a residue-by-residue basis. If the loss of conformational heterogeneity we detect in the R_ρ analysis (Table S2) is confirmed by other methods, this observation would suggest that the binding affinity of SpA^C for Fc is reduced by the entropic penalty associated with the suppression of conformational heterogeneity upon binding. It is easy to imagine ways that the evolved SpA sequence might have compensated for this entropic penalty. We previously hypothesized that the large extent of conformational heterogeneity in SpA domains might potentiate their binding promiscuity (16). Formally, this plasticity would come at an entropic cost to affinity to any one partner, but presumably allows *S. aureus* to use one surface protein to exquisitely enhance its virulence via multiple mechanisms of infection.

Experimental Procedures

Plasmid Construction. The SpA^C gene was PCR-cloned from the SpA-N gene. The PCR primers added 5′ NdeI and 3′ BamHI sites, and were subsequently cloned into the T7 expression plasmid pAED4 (32). The SpA^C Q9W plasmid was formed through site-directed mutagenesis of the wild-type SpA^C plasmid. The F_c gene of IgG was amplified from pEFc31 (18). The PCR primers added 5′ NcoI and 3′ XhoI sites that were used to subclone the F_c gene into pET28a (Novagen).

Protein Expression and Purification.

SpA^C proteins. SpA^C plasmids were transformed into *Escherichia coli* BL21(DE3) cells using a standard transformation procedure. A single colony of transformed bacteria was used to inoculate a 50-mL culture of Luria broth media with 0.1 mg/mL ampicillin. This starter culture was incubated at 37 °C until the optical density (OD) reached 0.8, whereupon it was used to inoculate a 1-L culture that was allowed to grow to OD 0.8 at 37 °C. Isopropyl-beta-D-thiogalactopyranoside (IPTG) was then added to a final concentration of 1 mM, and the culture was incubated for an additional 6–8 h. The cells were harvested by centrifugation at 6,700 × *g* and resuspended in 20–30 mL of 50 mM Tris (pH 8.8), 1 mM EDTA. The cells were lysed in a French pressure cell, and insoluble material was centrifuged from the lysate at 25,000 × *g*. The lysate was brought to pH 9.0, and micrococcal nuclease was added to digest large DNA fragments for 15 min. The resulting solution was brought to 4 M guanidinium HCl (Bio Basic). The solution was then dialyzed in a 5% (vol/vol) acetic acid buffer in two successive steps, which precipitated many cellular materials but not expressed SpA^C. After centrifugation of the insoluble material at 25,000 × *g*, the resulting solution was allowed to dialyze overnight into deionized water. SpA^C was further purified using a strong cation-exchanging SP Sepharose (GE Healthcare) column in 50 mM acetate buffer at pH 3.6. Protein was eluted with an NaCl gradient of typically 100–500 mM in a volume of 600–800 mL and collected in 10-mL fractions monitored by a UV detector (Bio-Rad) at 278 nm. Fractions comprising the protein elution peak were checked for purity by SDS/PAGE. The purest fractions were pooled and dialyzed against deionized water. The final solution was lyophilized and stored in a desiccator. The purity of the final protein stock was confirmed by SDS/PAGE to be >95% pure. The mass of SpA^C was confirmed with electrospray ionization mass spectroscopy.

F_c protein. The F_c plasmid was transformed into *E. coli* Rosetta-gami 2 B competent cells (EMD Millipore) using a standard transformation procedure. A single colony of transformed bacteria was used to inoculate a 5-mL culture of Luria broth media with ampicillin (100 μg/mL), chloramphenicol (35 μg/mL), and kanamycin (50 μg/mL). This starter culture was incubated at 37 °C for 24 h, whereupon 1 mL of this culture was used to inoculate a 200-mL culture. After 24 h of growth, the entirety of this culture was used to inoculate a 700-mL culture. IPTG was immediately added to a final concentration of 1 mM, and the culture was incubated for an additional 24 h. The cells were harvested by centrifugation at 6,700 × *g* and resuspended in 20 mL of 20 mM Tris (pH 8), 300 mM NaCl, 20% glycerol. The cells were lysed in a Microfluidizer (Microfluidics), and insoluble material was centrifuged from the lysate at 25,000 × *g*. The lysate was loaded on an Ni-NTA affinity column, washed with 20 mM Tris (pH 8), 500 mM NaCl, 20 mM imidazole, 20% glycerol, and eluted with 20 mM Tris pH (8), 100 mM NaCl, 200 mM imidazole in 5-mL fractions. The fractions comprising the protein elution peak were checked for purity by SDS/PAGE. The purest fractions were pooled and further purified using a Sephadex 200 size-exclusion column and eluted using 200 mL of 20 mM Hepes (pH 8), 50 mM NaCl in 1-mL fractions monitored by a UV detector at 280 nm. Peak fractions were checked for purity by SDS/PAGE. The purest fractions were pooled and concentrated.

Crystallization, Data Collection, Modeling, and Refinement. F_c and SpA^C proteins were mixed in a 2:1 molar ratio for 1 h at a concentration of 10 mg/mL complex. Each complex was mixed in a 1:2 ratio with crystallization solution (0.1 M NaOAc, pH 5.6, 0.1 M ammonium sulfate, 15% PEG 5K MME). Crystals of both complexes formed by sitting-drop vapor diffusion within 5 d at room temperature, and were of the space group *C*2. The SpA^C Q9W variant was mixed in a 1:1 molar ratio with crystallization solution (10 mM NaSCN, 18% PEG 3350). Crystals were each frozen by direct immersion in liquid nitrogen after addition of ethylene glycol to 20% (vol/vol). All data were collected remotely at the Advanced Photon Source (APS) at Argonne National Laboratory, beamline 22-ID (Southeast Regional Collaborative Access Team) at 100 K. Data were processed and scaled to 2.3-Å resolution with HKL2000 (33). Both structures of SpA^C in complex with F_c were solved using molecular replacement in Phaser (34) using PDB ID codes 4NPD (35) and 1FC2 (11). The SpA^C Q9W variant was solved using molecular replacement in Phaser using PDB ID code 4NPD (helices 2 and 3 only). All models were built in Coot (36). Refinement of all models was carried out in

phenix.refine (20). Refinement was performed using isotropic B factors for all atoms. Alternative conformations were modeled using qFit (24). The final refined complex models had R_{work}/R_{free} respective values of 21.1%/25.0% (PDB ID code 4WWI) and 19.6%/24.2% (PDB ID code 4ZNC). The final refined model for SpA^C Q9W (PDB ID code 4ZMD) had values of 19.9%/25.6%.

Quantitative ^3J Measurements. The scalar couplings of $^3J(C\gamma,C')$ and $^3J(C\gamma,N)$ for SpA^C were measured on an Agilent 800-MHz NMR spectrometer at 25 °C, using the J-modulated constant-time ^1H-^{13}C heteronuclear single quantum coherence experiment (22, 23). The reference and J-modulated spectra were recorded in an interleaved manner with a constant-time delay (2T) set to 57.4 ms to refocus the $^1J_{CC}$ coupling. The maximum evolution times for the ^{13}C and ^1H dimensions were 18.1 and 60 ms, respectively. The spectra were processed with NMRPipe (37) using the sine-bell window function for both dimensions, and the indirect dimension was zero-filled fourfold before Fourier transform. The peak intensities were measured by SPARKY (38), and the $^3J(C\gamma,C')$ and $^3J(C\gamma,N)$ couplings were calculated from the ratio of the peak intensities between the J-modulated spectrum (I_{mod}) and the reference spectrum (I_{ref}) by cos(2JT). The scalar couplings of $^3J(C\delta_1,C\alpha)$ and $^3J(C\delta_1,C\gamma_2)$ for the Ile residues were measured on an Agilent 800-MHz NMR spectrometer at 25 °C using the long-range ^{13}C-^{13}C correlation experiment reported previously (21) with minor modifications. The CO 180 refocused pulses during the two 2T periods were removed, and the CO composite pulse decouple was introduced during the t_1 evolution to remove $^1J(C\alpha,CO)$ coupling. The constant-time delay was set to 29.4 ms to refocus $^1J_{cc}$ couplings. The maximum evolution times were 4 and 80 ms for the ^{13}C and ^1H dimensions, respectively. Both dimensions were processed using the sine-bell window function, and the indirect dimension was zero-filled 16-fold before Fourier transform. All data were processed by NMRPipe (37), and peak volumes were obtained by automatic integration using the peakint module in the XEASY package (39). The $^3J(C\delta_1,C\alpha)$ and $^3J(C\delta_1,C\gamma_2)$ couplings were calculated from the ratio of the volumes of the long-range scalar coupled peaks V_c to the methyl signals V_0 by $-\tan^2(2\pi JT)$.

Isothermal Titration Calorimetry Studies. ITC experiments were performed using a MicroCal VP-ITC instrument (Malvern Instruments, Ltd.). All protein samples were prepared by extensive buffer exchange by dialysis against 20 mM Tris (pH 8), 100 mM NaCl. Experiments were performed by titrating F_c (100 μM) into SpA^C (5 μM), or SpA^C (100 μM) into F_c (5 μM), both at 25 °C with a stir speed of 307 rpm. Both isotherms were simultaneously fit to a binding model in Mathematica (Wolfram Research, Inc.) for wild-type SpA or Origin software (OriginLab Corp.) for the Q9W variant.

Illustrations. All structural illustrations were made in PyMOL (Schrödinger, LLC).

ACKNOWLEDGMENTS. We thank Charles Pemble for all of his assistance. Crystal screening and data processing were conducted in collaboration with the Duke Macromolecular X-Ray Crystallography Shared Resource. Diffraction data were collected remotely at the Southeast Regional Collaborative Access Team 22-ID beamline at the Advanced Photon Source, Argonne National Laboratory, supported by the US Department of Energy Sciences under Contract W-31-109-Eng-38. All other aspects of this work were supported by NIH Grant R01-GM081666 (to T.G.O.) and a grant from Duke University. The Henry and Dorothy Lingle Kamin Endowment Fund of the Triangle Community Foundation supported publication costs.

1. Lowy FD (1998) *Staphylococcus aureus* infections. *N Engl J Med* 339(8):520–532.
2. Murdoch DR, et al.; International Collaboration on Endocarditis-Prospective Cohort Study (ICE-PCS) Investigators (2009) Clinical presentation, etiology, and outcome of infective endocarditis in the 21st century: The International Collaboration on Endocarditis-Prospective Cohort Study. *Arch Intern Med* 169(5):463–473.
3. Fowler VG, Jr, et al. (2003) Clinical identifiers of complicated *Staphylococcus aureus* bacteremia. *Arch Intern Med* 163(17):2066–2072.
4. Gómez MI, O'Seaghdha M, Magargee M, Foster TJ, Prince AS (2006) *Staphylococcus aureus* protein A activates TNFR1 signaling through conserved IgG binding domains. *J Biol Chem* 281(29):20190–20196.
5. Gómez MI, et al. (2004) *Staphylococcus aureus* protein A induces airway epithelial inflammatory responses by activating TNFR1. *Nat Med* 10(8):842–848.
6. Hartleib J, et al. (2000) Protein A is the von Willebrand factor binding protein on *Staphylococcus aureus*. *Blood* 96(6):2149–2156.
7. O'Seaghdha M, et al. (2006) *Staphylococcus aureus* protein A binding to von Willebrand factor A1 domain is mediated by conserved IgG binding regions. *FEBS J* 273(21):4831–4841.
8. Lund LN, et al. (2011) Exploring variation in binding of protein A and protein G to immunoglobulin type G by isothermal titration calorimetry. *J Mol Recognit* 24(6):945–952.
9. Jansson B, Uhlén M, Nygren PA (1998) All individual domains of staphylococcal protein A show Fab binding. *FEMS Immunol Med Microbiol* 20(1):69–78.
10. Graille M, et al. (2000) Crystal structure of a *Staphylococcus aureus* protein A domain complexed with the Fab fragment of a human IgM antibody: Structural basis for recognition of B-cell receptors and superantigen activity. *Proc Natl Acad Sci USA* 97(10):5399–5404.
11. Deisenhofer J (1981) Crystallographic refinement and atomic models of a human Fc fragment and its complex with fragment B of protein A from *Staphylococcus aureus* at 2.9- and 2.8-Å resolution. *Biochemistry* 20(9):2361–2370.
12. Braisted AC, Wells JA (1996) Minimizing a binding domain from protein A. *Proc Natl Acad Sci USA* 93(12):5688–5692.
13. Kim HK, Cheng AG, Kim HY, Missiakas DM, Schneewind O (2010) Nontoxigenic protein A vaccine for methicillin-resistant *Staphylococcus aureus* infections in mice. *J Exp Med* 207(9):1863–1870.
14. Romagnani S, et al. (1982) Protein A reactivity of lymphocytes from some patients with chronic lymphocytic leukaemia mediated by an interaction with the F(ab')2 region of surface immunoglobulin. *Scand J Immunol* 15(3):287–295.
15. Kristiansen SV, Pascual V, Lipsky PE (1994) Staphylococcal protein A induces biased production of Ig by VH3-expressing B lymphocytes. *J Immunol* 153(7):2974–2982.
16. Deis LN, et al. (2014) Multiscale conformational heterogeneity in staphylococcal protein A: Possible determinant of functional plasticity. *Structure* 22(10):1467–1477.
17. Gouda H, et al. (1998) NMR study of the interaction between the B domain of staphylococcal protein A and the Fc portion of immunoglobulin G. *Biochemistry* 37(1):129–136.
18. Jendeberg L, et al. (1996) The mechanism of binding staphylococcal protein A to immunoglobin G does not involve helix unwinding. *Biochemistry* 35(1):22–31.
19. Torigoe H, Shimada I, Saito A, Sato M, Arata Y (1990) Sequential 1H NMR assignments and secondary structure of the B domain of staphylococcal protein A: Structural changes between the free B domain in solution and the Fc-bound B domain in crystal. *Biochemistry* 29(37):8787–8793.
20. Adams PD, et al. (2010) PHENIX: A comprehensive Python-based system for macromolecular structure solution. *Acta Crystallogr D Biol Crystallogr* 66(Pt 2):213–221.
21. Bax A, Max D, Zax D (1992) Measurement of long-range 13C-13C J couplings in a 20-kDa protein-peptide complex. *J Am Chem Soc* 114(17):6923–6925.
22. Grzesiek S, Vuister GW, Bax A (1993) A simple and sensitive experiment for measurement of JCC couplings between backbone carbonyl and methyl carbons in isotopically enriched proteins. *J Biomol NMR* 3(4):487–493.
23. Vuister GW, Yamazaki T, Torchia DA, Bax A (1993) Measurement of two- and three-bond 13C-1H J couplings to the C delta carbons of leucine residues in staphylococcal nuclease. *J Biomol NMR* 3(3):297–306.
24. van den Bedem H, Dhanik A, Latombe JC, Deacon AM (2009) Modeling discrete heterogeneity in X-ray diffraction data by fitting multi-conformers. *Acta Crystallogr D Biol Crystallogr* 65(Pt 10):1107–1117.
25. Hansen DF, Neudecker P, Vallurupalli P, Mulder FA, Kay LE (2010) Determination of Leu side-chain conformations in excited protein states by NMR relaxation dispersion. *J Am Chem Soc* 132(1):42–43.
26. Hansen DF, Neudecker P, Kay LE (2010) Determination of isoleucine side-chain conformations in ground and excited states of proteins from chemical shifts. *J Am Chem Soc* 132(22):7589–7591.
27. Lange OF, et al. (2008) Recognition dynamics up to microseconds revealed from an RDC-derived ubiquitin ensemble in solution. *Science* 320(5882):1471–1475.
28. Wilson MA, Brunger AT (2000) The 1.0 Å crystal structure of Ca(2+)-bound calmodulin: An analysis of disorder and implications for functionally relevant plasticity. *J Mol Biol* 301(5):1237–1256.
29. Wiseman T, Williston S, Brandts JF, Lin LN (1989) Rapid measurement of binding constants and heats of binding using a new titration calorimeter. *Anal Biochem* 179(1):131–137.
30. Tashiro M, et al. (1997) High-resolution solution NMR structure of the Z domain of staphylococcal protein A. *J Mol Biol* 272(4):573–590.
31. Nguyen T, Ghebrehiwet B, Peerschke EI (2000) *Staphylococcus aureus* protein A recognizes platelet gC1qR/p33: A novel mechanism for staphylococcal interactions with platelets. *Infect Immun* 68(4):2061–2068.
32. Doering DS (1992) Functional and structural studies of a small F-actin binding domain. PhD thesis (Massachusetts Institute of Technology, Boston).
33. Otwinowski Z, Minor W (1997) Processing of X-ray diffraction data collected in oscillation mode. *Methods Enzymol* 276:307–326.
34. McCoy AJ (2007) Solving structures of protein complexes by molecular replacement with Phaser. *Acta Crystallogr D Biol Crystallogr* 63(Pt 1):32–41.
35. Deis LN, et al. (2013) Phenix/MolProbity hydrogen parameter update. *Comput Crystallogr Newsl* 4:9–10.
36. Emsley P, Lohkamp B, Scott WG, Cowtan K (2010) Features and development of Coot. *Acta Crystallogr D Biol Crystallogr* 66(Pt 4):486–501.
37. Delaglio F, et al. (1995) NMRPipe: A multidimensional spectral processing system based on UNIX pipes. *J Biomol NMR* 6(3):277–293.
38. Goddard TD, Kneller DG (2004) SPARKY 3 (University of California, San Francisco).
39. Bartels C, Xia TH, Billeter M, Güntert P, Wüthrich K (1995) The program XEASY for computer-supported NMR spectral analysis of biological macromolecules. *J Biomol NMR* 6(1):1–10.

Supporting Information

Deis et al. 10.1073/pnas.1424724112

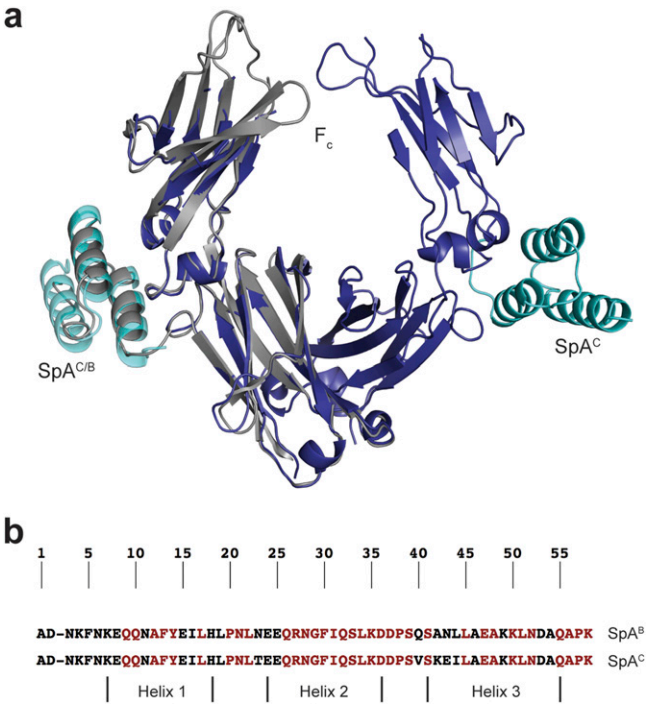

Fig. S1. Comparison between PDB ID codes 1FC2 and 4WWI, our new F_c–SpA^C complex structure. (*A*) SpA^B in 1FC2 binds to the same site on F_c as does SpA^C in the new complex. The F_c portions of both structures superimpose well. According to ref. 30, helix 3 in 1FC2 was folded irregularly and no density was observed, although nonhelical coordinates were still modeled. (*B*) SpA^B and SpA^C contain minimal sequence differences, none of which are interfacial. Red residues are identical in all five SpA protein binding domains.

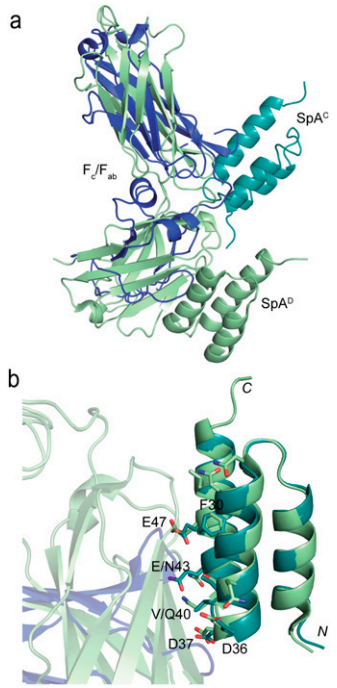

Fig. S2. SpA^C and F_c bind in a secondary mode. (*A*) SpA^C (dark cyan) binds to F_c (blue) in a different location from SpA^D binding to F_{ab} (green; from PDB ID code 1DEE). (*B*) The helix 2/3-binding sites on the SpA domain are nearly homologous, with only a few rotamer differences.

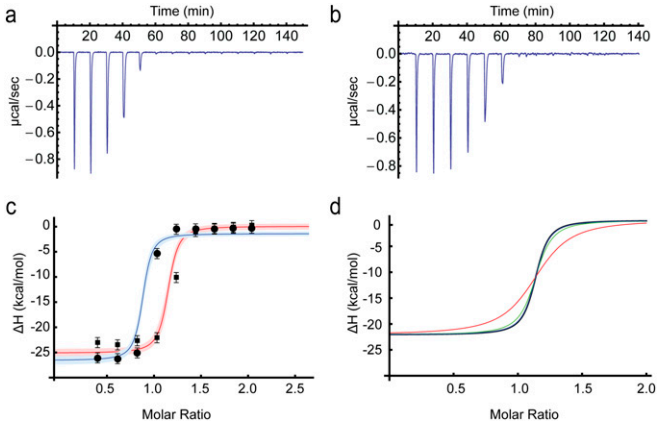

Fig. S3. Isothermal titration calorimetry data of SpA^C–F_c binding. (*A* and *B*) Raw data for (*A*) titration of 5 μM SpA^C with F_c and (*B*) titration of 5 μM F_c with SpA^C. (*C*) Best-fit ITC binding isotherms for titration of F_c into SpA^C (squares, red line) and SpA^C into F_c (circles, blue line). Bands represent 95% confidence intervals of best-fit isotherms. Error bars represent SEM. Best-fit parameter values (95% confidence interval) are K_a, 6.6 (5.6, 9.5) × 10^7 M^{-1}; ΔH, −25.4 (−25.8, −24.6) kcal/mol; n = 1.14 (1.13, 1.15). (*D*) Binding isotherms for titration of SpA^C with F_c were simulated using a two-site–binding model with the affinity, enthalpy, and n values given in *C*. Simulated single-site isotherm (black) and simulated two-site isotherms at various second-site K_d values: 1 μM (red), 10 μM (green), 100 μM (blue).

Table S1. Data collection and refinement statistics for the SpA^C–F_c complex

	SpA^C–F_c complex
Data collection	
Space group	*C*2
Cell dimensions	
a, *b*, *c*, Å	139.0, 88.1, 101.0
α, β, γ, °	90.0, 91.0, 90.0
Wavelength	1.0
Resolution, Å	50.00–2.30 (2.34–2.30)*
R_{sym}	0.17 (1.0)
$I/\sigma I$	29.0 (1.7)
Completeness, %	99.5 (94.8)
Redundancy	14.8 (12.3)
Refinement	
Resolution, Å	41.18–2.31
No. of reflections	50,556
R_{work}/R_{free}	21.2/25.0
No. of atoms	
Protein	6254
Water	165
B factors	
Protein	62.96
Water	76.44
Rms deviations	
Bond lengths, Å	0.004
Bond angles, °	0.817

*Data were collected from a single crystal. Values in parentheses are for the highest-resolution shell.

Table S2. R_ρ for apo SpA^C and SpA^C in complex with F_c

Residue	Apo (4NPD)	Complex (4WWI) chain A	$\frac{R_\rho^{apo}-R_\rho^{cmplx}}{R_\rho^{apo}}$, %	Residue	Apo (4NPD)	Complex (4WWI) chain A	$\frac{R_\rho^{apo}-R_\rho^{cmplx}}{R_\rho^{apo}}$, %
N3	0.59	0.25	58	F30	1.01	0.20	80
K4	0.88	0.80	9	I31*	0.81	0.26	68
F5	0.98	0.45	55	Q32	0.77	0.30	61
N6	0.98	0.12	88	S33	1.00	0.28	72
K7	0.67	0.58	13	L34	0.59	0.07	88
E8	0.70	0.72	−3	K35	0.58	0.29	50
Q9	0.69	0.12	83	D36	0.47	0.06	87
Q10*	0.74	0.16	78	D37	0.98	0.06	94
N11	0.43	0.91	−112	P38	0.52	0.53	−2
F13*	0.79	0.14	82	S39	0.77	0.44	43
Y14*	0.93	0.01	99	V40	0.78	0.50	36
E15	0.65	0.78	−20	S41	0.85	0.27	68
I16	0.85	0.18	79	K42	0.49	0.60	−22
L17*	0.80	0.02	98	E43	0.72	0.28	61
H18*	0.97	0.11	89	I44	0.79	0.45	43
L19	0.88	0.04	95	L45	0.85	0.38	55
P20	0.75	0.33	56	E47	0.94	0.57	39
N21	0.82	0.08	90	K49	0.84	0.35	58
L22	0.95	0.19	80	K50	0.59	0.50	15
T23	0.95	0.43	55	L51	0.87	0.20	77
E24	0.59	0.50	15	N52	0.94	0.39	59
E25	0.59	0.60	−2	D53	0.68	0.23	66
Q26	1.00	0.16	84	Q55	1.00	0.19	81
R27	0.88	0.36	59	P57	0.84	0.15	82
N28	0.60	0.12	80	K58	0.35	0.47	−34

Statistics comparing interfacial and noninterfacial residues

Residue type	Apo mean	Complex mean	$\frac{R_\rho^{apo}-R_\rho^{cmplx}}{R_\rho^{apo}}$, %	
All	0.77 (0.17)[†]	0.32 (0.22)	53 (42)	
Interfacial	0.84 (0.09)	0.12 (0.09)	86 (12)	} $P = 0.00007$[‡]
Noninterfacial	0.76 (0.18)	0.35 (0.22)	48 (42)	

It is difficult to quantitatively estimate the uncertainty in electron-density values; therefore, we have not included uncertainties in R_ρ. Qualitatively, sources of error that contribute to uncertainty in electron density and therefore R_ρ include data collection errors, crystal defects, modeling errors, and refinement artifacts.

*Interfacial residues.

[†]Numbers in parentheses are SDs.

[‡]Based on a Student *t* hypothesis test. The *P* value is the probability that interfacial and noninterfacial residues have the same reductions in conformational heterogeneity upon F_c binding.

Table S3. Comparison of NMR and crystallographic observations of conformational heterogeneity

Residue	Apo (X-ray)*	Apo (NMR)†	^{3}J(Hz)	Chemical shift	Complex (X-ray)*	Complex ρ ratio‡	Note
K4	χ_1: +	χ_1: +	$^3J(C\gamma C') = 2.72 \pm 0.01$		χ_1: +	0.57	
K7	χ_1: +	χ_1: +	$^3J(C\gamma C') = 2.61 \pm 0.01$		χ_1: +	0.45	
I16	χ_1: −	χ_1: −	$^3J(C\gamma_1 C') = 3.95 \pm 0.05$	$C(\delta_1) = 13.7$ ppm	χ_1: −	0.07	From NMR scalar coupling and chemical shift:
	χ_2: −	χ_2: +	$^3J(C\gamma_1 N) = 0.37 \pm 0.21$;		χ_2: −		Population trans 0.80
			$^3J(C\gamma_2 C') = 1.09 \pm 0.01$;				Population gauche− 0.20
			$^3J(C\gamma_2 N) = 2.10 \pm 0.01$				
L17§	χ_1: a	χ_1: +	$^3J(C\gamma C') = 2.97 \pm 0.02$	$C(\delta_1) = 24.7$ ppm	χ_1: −	0.24	
	χ_2: a	χ_2: +	$^3J(C\gamma N) = 0.74 \pm 0.07$	$C(\delta_2) = 23.0$ ppm; $\Delta CS = 1.7$ ppm	χ_2: −		
L19	χ_1: −	χ_1: −	$^3J(C\gamma C') = 3.80 \pm 0.04$;	$C(\delta_1) = 26.6$ ppm	χ_1: −	0.13	
	χ_2: a	χ_2: +	$^3J(C\gamma N) = 0.73 \pm 0.20$	$C(\delta_2) = 22.8$ ppm; $\Delta CS = 3.8$ ppm			
L22	χ_2: −	χ_2: −		$C(\delta_1) = 27.2$ ppm; $C(\delta_2) = 22.2$ ppm; $\Delta CS = 5.0$ ppm	χ_2: −	0.3	
T23	χ_1: −	χ_1: +	$^3J(C\gamma_2 C') = 3.06 \pm 0.01$; $^3J(C\gamma_2 N) = 1.08 \pm 0.01$		χ_1: −	0.1	Crystal contact
I31§	χ_1: −	χ_1: −	$^3J(C\gamma_1 C') = 3.72 \pm 0.03$;	$C(\delta_1) = 12.4$ ppm	χ_1: −	0.13	
	χ_2: m	χ_2: +	$^3J(C\gamma_1 N) = 0.36 \pm 0.20$		χ_2: −		
L34	χ_2: +	χ_2: +		$C(\delta_1) = 25.5$ ppm $C(\delta_2) = 25.4$ ppm; $\Delta CS = 0.1$ ppm	χ_2: +	0.63	
V40	χ_1: −	χ_1: −	$^3J(C\gamma_1 C') = 1.05 \pm 0.01$; $^3J(C\gamma_1 N) = 0.72 \pm 0.01$; $^3J(C\gamma_2 C') = 3.65 \pm 0.01$; $^3J(C\gamma_2 N) = 0.45 \pm 0.02$		χ_1: −	0.10	
I44	χ_1: −	χ_1: −	$^3J(C\gamma_1 C) = 3.60 \pm 0.02$;	$C(\delta_1) = 13.0$ ppm	χ_1: −	0.22	
	χ_2: a	χ_2: +	$^3J(C\gamma_1 N) = 0.52 \pm 0.15$; $^3J(C\delta_1 C\alpha) = 2.77 \pm 0.01$		χ_2: +		
L45	χ_1: −	χ_1: ?		$C(\delta_1) = 23.8$ ppm	χ_1: −	0.26	From NMR chemical shifts:
	χ_2: −	χ_2: −		$C(\delta_2) = 24.5$ ppm; $\Delta CS = -0.7$ ppm	χ_2: −		Population trans 0.43 Population gauche+ 0.57
K49	χ_1: −	χ_1: −	$^3J(C\gamma C') = 3.57 \pm 0.03$		χ_1: −	0.29	
	χ_2: +	χ_2: N			χ_2: +		
L51	χ_1: +	χ_1: ?		$C(\delta_1)$,$C(\delta_2) = 24.1$ ppm; $\Delta CS = 0$ ppm	χ_1: −	0.44	
	χ_2: +	χ_2: +			χ_2: +		

*+, conformational heterogeneity observed in crystal structure; −, no conformational heterogeneity observed; a, anisotropic electron density observed; m, multiple rotamers observed among different apo SpA-domain structures.

†Dynamic side chains as detected by ^{3}J averaging and/or chemical shift deviations from static limits; +, dynamic χ_1 or χ_2; −, static χ_1 or χ_2; N, no observation; ?, ambiguous assignment.

‡Values close to 0 indicate low conformational heterogeneity; values close to 1 indicate high conformational heterogeneity (see text).

§Residues that make contact with F_c.

Table S4. Data collection and refinement statistics for SpA^C Q9W

	SpA^C Q9W
Data collection	
Space group	$P6_5$
Cell dimensions	
a, *b*, *c*, Å	44.5, 44.5, 116.1
α, β, γ, °	90.0, 91.0, 120.0
Wavelength	1.0
Resolution, Å	50.00–1.87 (1.90–1.87)*
R_{sym}	0.091 (0.72)
$I/\sigma I$	123.5 (2.6)
Completeness, %	99.9 (100.0)
Redundancy	17.0 (10.5)
Refinement	
Resolution, Å	36.6–1.87
No. of reflections	9,603
R_{work}/R_{free}	19.9/25.6
No. of atoms	
Protein	921
Water	22
B factors	
Protein	59.3
Water	69.5
Rms deviations	
Bond lengths, Å	0.013
Bond angles, °	1.189

*Data were collected from a single crystal. Values in parentheses are for the highest-resolution shell.

Table S5. Data collection and refinement statistics for SpA^C Q9W in complex with F_c

	SpA^C Q9W–F_c complex
Data collection	
Space group	*C*2
Cell dimensions	
a, *b*, *c*, Å	138.0, 87.2, 103.2
α, β, γ, °	90.0, 91.1, 90.0
Wavelength	1.0
Resolution, Å	50.00–2.28 (2.32–2.28)*
R_{sym}	0.137 (1.0)
$I/\sigma I$	19.9 (1.6)
Completeness, %	100.0 (99.8)
Redundancy	7.9 (6.2)
Refinement	
Resolution, Å	34.8–2.28
No. of reflections	52,860
R_{work}/R_{free}	19.6/24.2
No. of atoms	
Protein	6,197
Water	126
B factors	
Protein	61.91
Water	53.28
Rms deviations	
Bond lengths, Å	0.016
Bond angles, °	1.506

*Data were collected from a single crystal. Values in parentheses are for the highest-resolution shell.